Journal of
Advanced
Science and
Research

Thickness Dependent Photoluminecsence and Photocatalytic Properties of Hydrothermally Prepared Sol-Gel Dip Coated Nanocrystalline TiO_2 Thin Films

Sayari Biswas[1]; Kazi Hasibur Rahman[2]; Asit Kar[3]

[1,3] *Micro and Nanoscience Laboratory, Department of Applied Physics, Indian Institute of Technology (Indian School of Mines), Dhanbad - 826004, Jharkhand, India.*

[2]*Swami Vivekananda University, Kolkata, India*

Abstract: Titanium dioxide (TiO_2) thin films were synthesized by sol-gel dip coating method on ITO coated glass substrate. The TiO_2 sol was prepared by hydrothermal method at two different temperatures, viz. 90 °C and 180 °C. It was then used to deposit the films by dip coating method. Each film was made by repeating the dipping cycle 2 ─ 12 times with constant dipping and lifting speed. Afterwards they were annealed at 500 °C for 6 h. XRD peaks confirm the anatase phase formation for all the samples. Crystallite size increases with increasing sol preparation temperature and also with increasing number of coating cycles. Abrupt rise spectra of transmission was observed in the violet-ultraviolet transition region and a maximum transmittance of ~55% was attained for as-deposited sample made from 90 °C sol. Band gap of the prepared films varies from 2.85 eV to 3.24 eV as the thickness and sol preparation temperature varies. FESEM images reveal that the films consisting spherical nanoparticles with varying size ranging from 15 nm to 8 nm and they are not homogeneous in terms of thickness. So they exhibit varying RMS roughness when studied by AFM. Photocatalytic activities of the films increase as their thickness increase.

Contents available at:
https://www.swamivivekanandauniversity.ac.in/jasr/

Cite this article: Sayari Biswas; Kazi Hasibur Rahman; Asit Kar,2025, Thickness Dependent Photoluminecsence and Photocatalytic Properties of Hydrothermally Prepared Sol-Gel Dip Coated Nanocrystalline TiO_2 Thin Films; Volume 1 (Issue 1): Pages 1-21.
DOI: 10.29322/IJSRP.X.X.2025.pXXXX

Received: 30. August 2024

Accepted: 28 November 2024

Keywords: Titanium dioxide, AFM, Sol-Gel, Band gap, Crystallite size

Authors for correspondence:
Author Name: Sayari Biswas[1], Kazi Hasibur Rahman[2]
e-mail: [1]sayaribiswas@gmail.com
[2]via.kazi786@gmail.com

1. Introduction:

For quite a long time titanium dioxide (TiO_2) nanoparticles are the prime attraction of a large number of researchers for a variety of novel properties. It is non-toxic and chemically stable. It has a low production cost and unique physio-chemical properties. Being a wide band gap semiconductor, TiO_2 possesses interesting electronic properties along with the possibility of easy nanostructuring. TiO_2 finds its usefulness in a variety of applications like dye-sensitized solar cell[1,2,] photo catalysis[3], electronic device fabrication[4], energy storage[5], environmental purification[6], photo-induced water disinfection[7], gas sensor[8], memory devices[9] etc. It also has the potential use in white pigment production[10], corrosion protective multilayer mirror[11], and antireflection coatings[12]. Due to enhanced surface area, nanostructured TiO_2 plays a crucial role in improving the performance of several kinds of devices.

These noble properties of TiO_2 get even enhanced in the form of thin film in nanometric scale mainly due to enormous effective surface area. This surface area enhancement is even higher if the thin films have a multilayer structure. Multilayer thin films have been proved to be a convenient tool for enhancing various properties of material like sensitivity to oxygen gas and volatile organic compounds, antireflection properties, ability of self cleaning etc. Thin multilayer films are deposited mainly by sputtering, vacuum evaporation, chemical vapour deposition (CVD), atomic layer deposition (ALD) etc. However, these methods have some disadvantages like high production cost and the requirement of specialized apparatuses for deposition of films. In this situation sol-gel method comes up to be a possible solution. Negishi *et. al.* used diethylene glycol (DEG) and polyethylene glycol (PEG) as additives to prepare transparent TiO_2 thin films via sol-gel method [13]. Yu et. al. prepared TiO_2 thin films with different surface structures from alkoxide solutions containing polyethylene glycol (PEG) via sol-gel method[14]. In another report they presented sol-gel preparation of transparent TiO_2 thin film with high photocatalytic activity, also via sol-gel mothod[15]. Garzella et. al. reported fabrication of Thin composite films of TiO_2 via the chemically modified sol–gel technique by dip-coating onto alumina substrates. Wang et. al. spin coated TiO_2 thin film on Si (100) substrates via an aqueous sol–gel route using Titanium butoxide precursor[16]. Kasuga *et al*. adopted an alkali hydrothermal method to prepare titanate nanotubes without using any template[17]. They obtained needle-shaped anatase TiO_2 crystals treating sol-gel-derived fine TiO_2-based powders with NaOH aqueous solution. Ichinose *et al*.[18] have reported the preparation of peroxo-modified sol of anatase TiO_2 using peroxo-titanium acid (PTA) solution by the mixture of $TiCl_4$ and H_2O_2 solution. PTA sol is an economic way for making low-temperature (~100 °C) TiO_2 coating with high substrate adhesion and high transmittance. Lee *et al*.[19] prepared PTA sol using $TiCl_3$ and dip-coated it on various substrates like slide glass, quartz and silicon wafer.

As mentioned earlier, one of the most versatile applications of TiO_2 now-a-days is the photocatalytic degradation of environmental pollutants due to its excellent thermal[20,21] and photostability[22] and high oxidizing capability of the generated holes. But the powder forms of these photocatalysts restrict their use in the industrial application. For the achievement of high photocatalytic conversion rates, a large specific surface area is of prime need. This can be achieved by dispersing nanoparticles (NPs) in suspensions or by placing them on a substrate and thus also overcoming the industrial limitations of nanopowders. Recently development of thin film photocatalysts has open a new direction for their use as self cleaning glasses and antibacterial ceramic materials for air cleaners[23,24]. Morphology and crystal structure of TiO_2 nanoparticles plays a crucial role in their photocatalytic activity. Generally anatase TiO_2 outfight rutile in this matter, although the reverse one has also been reported in few cases[25,26]. Thus photocatalytic activity of anatase TiO_2 has become the prime attraction of the researchers around the globe. Scientists are trying to tune the morphology, crystal structure, band gap, dopants etc. to improve the activity. But only a few reports are available on the detailed optical and photocatalytic study of TiO_2 thin films with varying thicknesses.

The present study has been focused on repeating thin layers of TiO_2 deposited on ITO coated glass substrate by hydrothermal assisted sol-gel dip coating method. We prepared PTA sol and treated it hydrothermally in a teflon lined autoclave at two different temperatures to prepare the final sol for TiO_2 film deposition. Thin films were prepared from sol made at both temperatures with 2, 6 and 12 layers and studied their optical and structural properties.

2. Materials & Method

2.1 Chemicals:

In this work, titanyl sulphate [$TiOSO_4$], Ammonia [NH_4OH, 3molL^{-1}] and Hydrogen peroxide [30% H_2O_2] were used as starting materials. All the chemicals used in this work are of Reagent Grade. First two chemicals were purchased from Sigma Aldrich and the other one from Avra Chemicals. ITO coated glass substrates were supplied by Macwin India Pvt. Ltd.

2.2 Synthesis:

TiO_2 thin films were deposited on ITO coated glass substrate using sol-gel dip coating method (Apex XDip-SV1 dip coater). To prepare the sol, Titanyl sulphate ($TiOSO_4$), was slowly dissolved in distilled water at room temperature27 and ammonia [NH4OH, 3molL^{-1}] was added in the solution. It results in the white precipitate of titanium hydroxide [$Ti(OH)_4$]. This precipitation was collected and washed repeatedly with distilled water using a filter paper to remove excess NH^{4+} and SO^{4-} ions. The white residue on the filter paper was then homogeneously dispersed in distilled water and peptized with 30% H_2O_2 under continuous magnetic stirring. After 20 h Peroxo Titanic Acid (PTA) sol was obtained. The sol was put in a Teflon lined stainless steel autoclave for thermal treatment in an oven. Two thermally treated sols were separately prepared at two different temperatures, viz. 90 ºC and 180 ºC for 12 h each. This final sol was used to deposit the thin films. Dipping and lifting speeds were constant at 20 mm/min. The used substrates were cleaned ultrasonically by acetone and isopropyl alchohol. Samples were deposited with 2, 6 and 12 numbers of coating cycles, i.e. with different thicknesses from both the sols. Then the films were dried at 60 ºC for 30 minutes in a hot air oven and were annealed at 500 ºC in a furnace for 6 h.

2.3. Characterizations:

The crystallinity and phase of the thin films were determined by X-ray diffraction (XRD) study in Grazing Incidence (GI) mode between 10° and 90° at by a PANlytical X'Pert ultra fast diffractometer with CuKα1 (λ = 0.154 nm) radiations.

Fourier transform infrared spectroscopy was done in the range 400 – 4000 cm–1 by Shimadzu IRAffinity-1. Since glass is opaque to IR below the wavelength 2000 cm^{-1}, the FTIR spectra was collected in ATR mode with an incidence angle of 10°.

To determine the defect levels in the synthesized TiO2 films, Photoluminescence emission spectra was recorded in the wavelength range 300 nm – 600 nm with an excitation wavelength of 260 nm on a Horiba-2500 Acton Fluorescence Spectrometer with a 150 W Xe lamp. Absorption and transmission spectra of the deposited films were collected using Agilent Cary 5000 UV-Vis spectrophotometer.

Morphological studies of the surface of the films were studied by FE-SEM Supra 55 and Dimension ICON Atomic Force Microscopy (Bruker). From FESEM images histogram of particle size distributions have been constructed using ImageJ software.

The photocatalytic activity of the prepared thin films was analyzed by decomposition of aqueous solution of Methylene Blue (MB) dye. Initially, 1.5×10^{-6} M Methylene Blue was added in to 100 ml of DI water and stirred for 15 minutes. The TiO2 thin films were placed inside the solution vertically with the help of a copper holder and exposed under UV light. All the films had a coating area of 1.5 cm × 1 cm. 5 ml of the solution was taken from the total solution at the regular interval of 15 min until a total duration of 90 min. UV-Vis absorbance spectra of the collected solutions were recorded with an Ocean Optics DH–2000–BAL UV-Vis spectrophotometer in the range 500 nm – 800 nm to evaluate the degradation rate of the dye.

3. Result and Discussion

3.1 Crystal Structure:

The XRD profiles of the TiO_2 thin films are shown in figure 1. For better clarity and ease of comparative analysis the XRD profiles have been shifted along y-axis with appropriate values. All the samples were found to be anatase with (101) being the dominant plane. The XRD profiles did not show the presence of any other phase or form of TiO_2 in all the samples. The sol for our thin films was made in an autoclave under high pressure. At high pressure, high density negative oxygen ions are movable which impart high energy to the atoms. This is another reason for the observed crystalline nature of our samples.

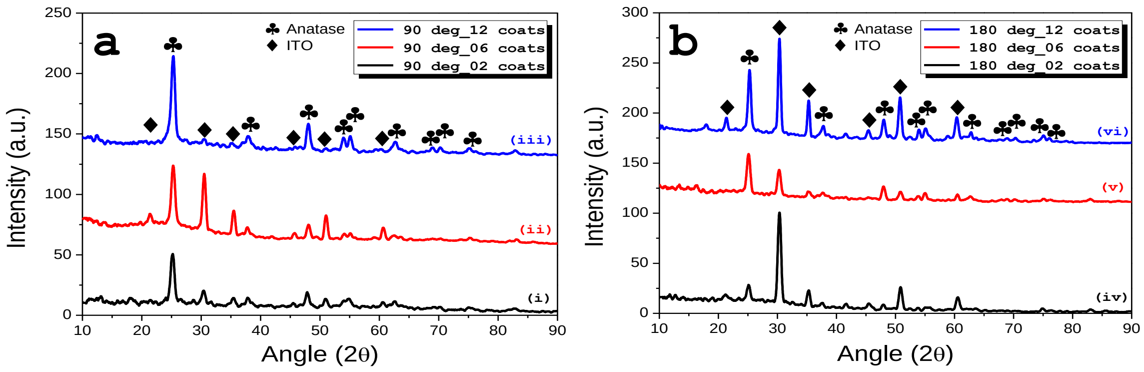

Figure 1: XRD profiles of (a) samples made from 90 °C sol (b) samples made from 180 °C sol

From the full width at half maximum (FWHM) of the XRD peaks of TiO2 the crystallite size was calculated from peaks using the Williamson-Hall equation[28]:

$$\mathrm{l}\cos\theta = \frac{K\lambda}{D} + 4\varepsilon\sin \qquad (1)$$

Here βhkl is the width of each peak at half of its maximum intensity (FWHM), K=0.94, λ is wavelength of incident radiation = 0.1542 nm and D is the desired crystallite size. The intercept to y-axis of the straight line fit of βhklcosθ/λ vs sinθ/λ curve gives the crystallite size for all the samples. For sample prepared from 90 °C sol crystallite size (D1) was found to be 5.8 nm, 6.2 nm and 6.2 nm for films with 2 coatings, 6 coatings and 12 coatings respectively. For the sample prepared from 180 °C the values were 6 nm, 6.9 nm and 7.1 nm. As the sol preparation temperature increases, the increased thermal energy of the system allows the grain boundaries grow that finally ends up in bigger crystallite size of the TiO_2 particles. When number of layers increases, it creates a chance for more and more crystallite to stick together to form a bigger one.

3.2 FTIR:

Figure 2 shows the FTIR spectra of thin films prepared with 12 coatings of sol. The TiO_2 samples show several bands in the range 400 – 700 cm-1, which are attributed to Ti-O stretching and Ti-O-Ti bridging stretching modes. The FTIR spectra confirm the presence of Ti—O vibrational band at 857 cm-1 which is due to the presence of $[TiO_4]^{-4}$ tetrahedral units. At 1105 cm^{-1} —C—O stretching vibration was observed29. The Peaks at 1562 and 1464 cm^{-1} correspond to the symmetric and asymmetric stretching vibrations of C(=O)O- group30. The absorptions at 1660 cm^{-1} and 1735 cm^{-1} are due to C=O and C=O bending vibrations respectively. The C=O appeared as the trace of organic compounds used during the synthesis process. The IR bands at 3750 and 3850 cm-1 show the presence of –OH stretching vibrations and the N-H vibration for NH^{4+} ions respectively[31,32]. Presence of nitrogen indicates the use of ammonium hydroxide for the synthesis of TiO_2. –OH stretching vibrations occur due to intermolecular interactions of $H_2O\cdots H_2O$ and $Ti–OH\cdots H_2O$[33]. This OH radical mainly resides on the octahedral sites of the TiO_2 lattice and actively participate in photocatalytic activity. Increasing intensity of this peak indicates towards better photocatalytic activity.

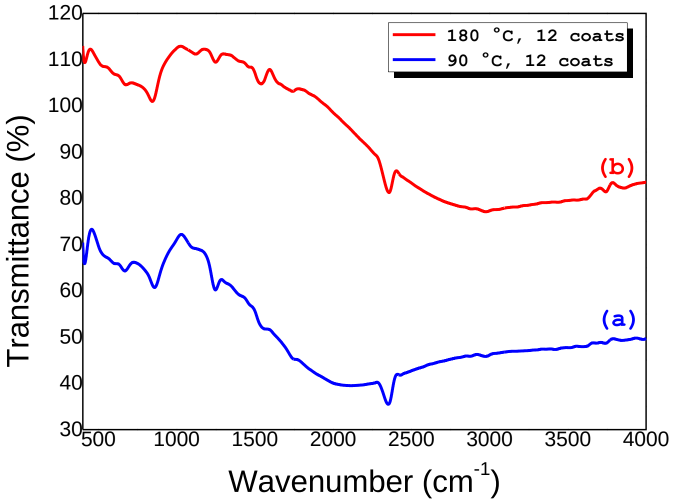

Figure 2: FTIR spectra of samples with 12 numbers of coatings made from sol prepared at (a) 90 °C and (b) 180 °C.

3.3 FESEM:

Figure 3 shows FESEM top views of the annealed films with 2, 6 and 12 numbers of coatings, prepared from both the sols (90 °C and 180 °C) together with histograms of the particle size distributions of the corresponding samples. Irrespective of sol preparation temperature and number of coatings, all the samples consist of spherical or almost spherical nanoparticles. As an effect of the high temperature and pressure the nano granules stick to each other to form agglomerated nanoparticles, with diameter ranging from 15 to 85 nm. During film deposition, when the substrate is dipped into the sol, agglomerated TiO_2 particles gets sticked over the substrate and during drying they form the film. These agglomerations are only visible in the FESEM images.

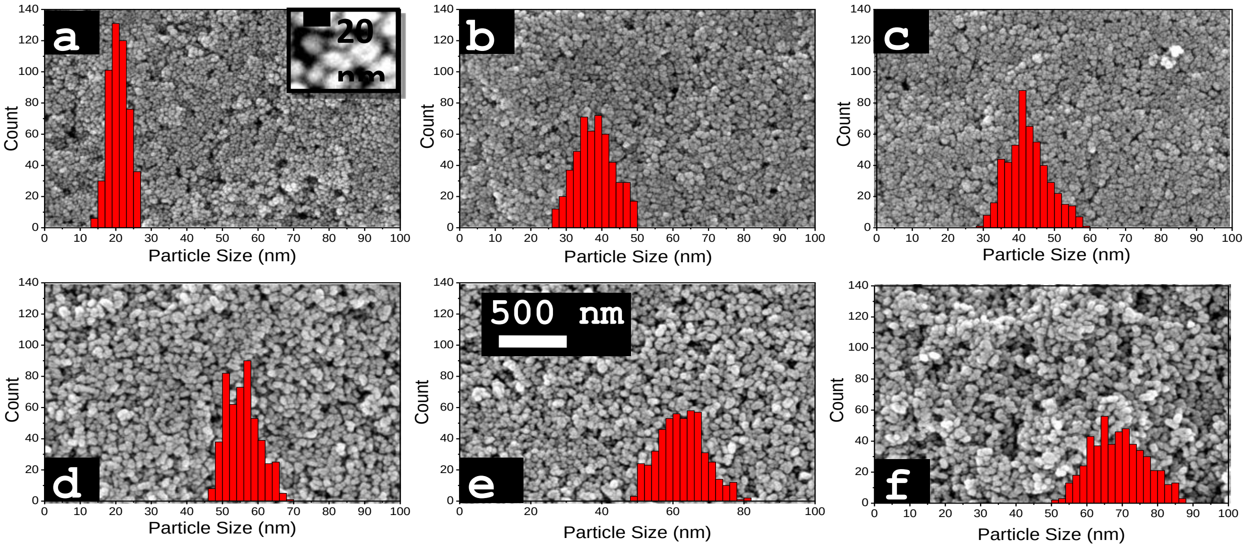

Figure 3: FESEM top view and particle size histogram of samples made from 90 °C sol (a) 2 coats (b) 6 coats (c) 12 coats and samples made from 180 °C sol (d) 2 coats (e) 6 coats (f) 12 coats. (Inset) magnified view of (a)

The spontaneous nucleation under hydrothermal conditions leads to aggregation of nucleating particles and in our case it takes the spherical shape. Generally, during particle formation it takes the shape (in nano regime) where it acquires minimum free energy. Spheres have minimum surface area for a given volume. So, to minimize the surface energy, it takes the spherical shape in the given thermal condition. Our samples were prepared in hydrothermal system under high pressure which restricts the volume growth from all the sides. It also leads to the formation of spherical particles. In this case the particles grow in volume to compensate the increased thermal energy due to increased temperature. The Hall Williamson plot from XRD profile also supports the result revealing increment in crystallite size as well.

The distribution of spherical nanostructures on the surface of the films prepared from 90 °C sol is relatively homogeneous in comparison to films prepared from 180 °C sol. For the second case (samples made from 180 °C sol) larger agglomerations were observed. For the thin films prepared from 90 °C sol the size varies as the number of coatings increases from 2 to 12. For film with 2 coats of sol, agglomeration diameter is ~15–25 nm. When the coatings are increased to 6 and 12, the agglomerated particle size (or diameter) increases to ~35–45 nm. For the thin films prepared from 180 °C sol, particle size change in the similar manner. With increase in coating numbers, the films show increase in diameter from 50 nm to 85 nm. But comparing films with same no of coating cycles, it was observed that the particle size increases when the sol preparation temperature increases and this increment is more prominent with lower number of coatings. For example, the average diameter increases from ~60 nm to ~75 nm for samples with 12 coatings when sol preparation temperature increases from 90 °C to 180 °C. For 2 numbers of coatings this increment is from ~20 nm to ~50 nm. Another important feature observed is that the distribution is narrower for thinner samples made from both the sols and this feature is clearly visible in the histograms. The histograms also show horizontal shifting of particle size towards higher value with increase in film thickness. For thinner films histograms are more symmetric with respect to their mid value. Average particle size for each film has been shown graphically in figure 4.

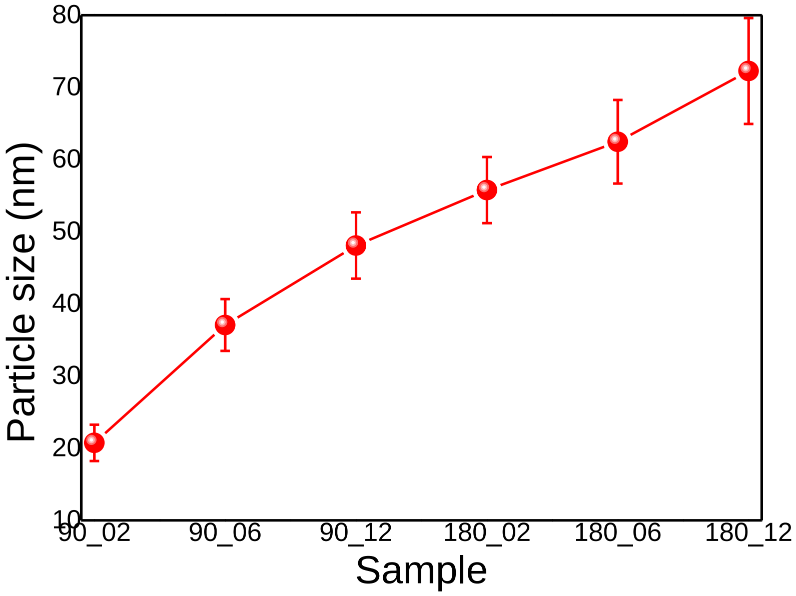

Figure 4: Average particle size determined using ImageJ software from FESEM top view of 90 °C sol (a) 2 coats (b) 6 coats (c) 12 coats and samples made from 180 °C sol (d) 2 coats (e) 6

With increased hydrothermal temperature, presence of some small voids was observed in all the samples. Since samples grown at 90 °C have lower particle size, their growth is more uniform than samples grown at 180 °C. Smaller particles easily get fitted into the interstitial voids of the previous layer. In fact for 90 °C samples, films with only 2 coatings have more voids which was later compensated due to the addition of particles from next layers. But for larger particles, the interstitial sites are not enough to fit them. So, they tend to sit on the particle sites of the previous layers. That's why, in the samples made from 180 °C sol, void are clearly seen in FESEM images. These voids provide additional effective surface area and roughness.

Table 1: Measured crystallite size (from XRD), average particle size and particle size distribution

Sample Name	AvgCrystallite (nm)	Avg particle size (nm)	Standard Daviation of particle size (nm)	Size range (nm)
90 deg_2 coats	5.8	21	2.5	13—27 = 14
90 deg_6 coats	6.2	37	3.6	26—50 = 24
90 deg_12 coats	6.2	48	4.6	30—58 = 28
180 deg_2 coats	6.0	58	4.6	46—68 = 22
180 deg_6 coats	6.9	62	5.8	48—82 = 34
180 deg_12 coats	7.1	72	7.3	50—88 = 38

We also studied the cross sectional view of the thin films. In all the images (Figure 5), a clear view of the film on the substrate can be seen.

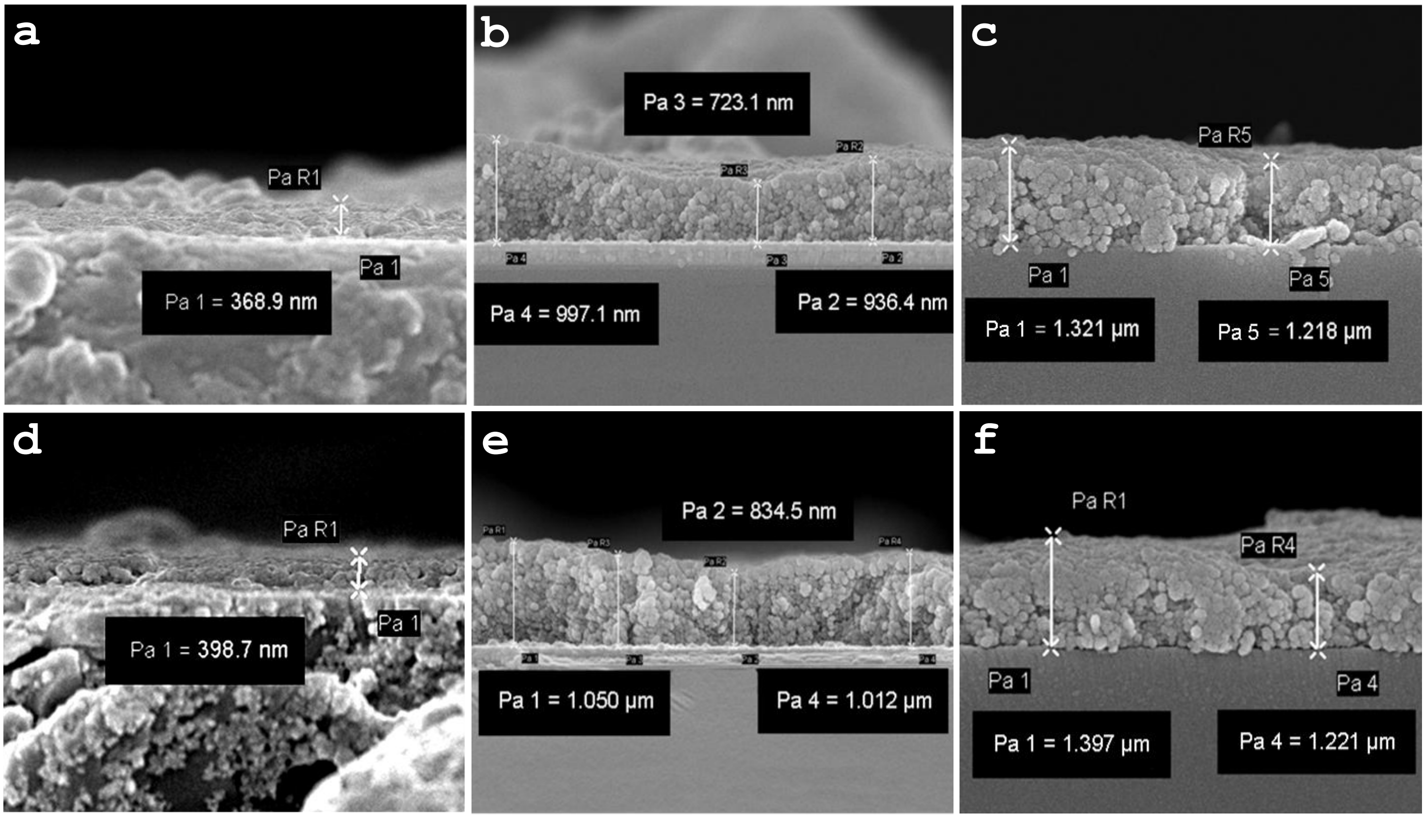

Figure 5: FESEM cross-sectional images of samples made from 90 °C sol (a) 2 coats (b) 6 coats (c) 12 coats and samples made from 180 °C sol (d) 2 coats (e) 6 coats (f) 12 coats

Film thickness increases with number of coating cycles, as expected. But this increase is not uniform. When numbers of coating cycles are increased from 2 to 6, the film thickness increases by almost 600 nm. But for the next one, i.e. films with 12 numbers of coating cycles, the increment in thickness is almost 300 nm. The cross section images show that the synthesized film surfaces are not at all uniform. As in the top view, the spherical nature of the particles is prominent in the cross section views too. With increasing thickness, small voids between the spherical particles are seen which occurred due to the layered structure of the films. Careful analysis reveals that homogeneity in thickness of deposited films improves with increased thickness of the film. For thinner films, surface atoms are subjected to form a weak inter-atomic force so as to form a loose packed structure. The compactness of the deposited films increases with increase in thickness of the films. This is caused by stronger inter-atomic forces at deeper layers. It is evident from FESEM images that surface morphology of all deposited films is almost uniform, homogenous and crack free.

3.4 Atomic Force Microscopy:

An Atomic Force Microscope (Dimension Icon) in contact mode was used to examine the surface morphology of the deposited films. Three-dimensional (3D) AFM images (Figure 6) show that the surface of the TiO_2 films has the shape of hills and valleys. 2D images reveal that (not shown here) the films of uniformly distributed granular particles. A large number of scans were executed randomly keeping the scanned area constant at 1 μm × 1 μm. The data were analyzed by NanoScope software (Version 1.4) to obtain the value of different parameters like the root mean square roughness (Rq), average roughness (Ra), surface skewness (Rsk) and kurtosis (Rku).

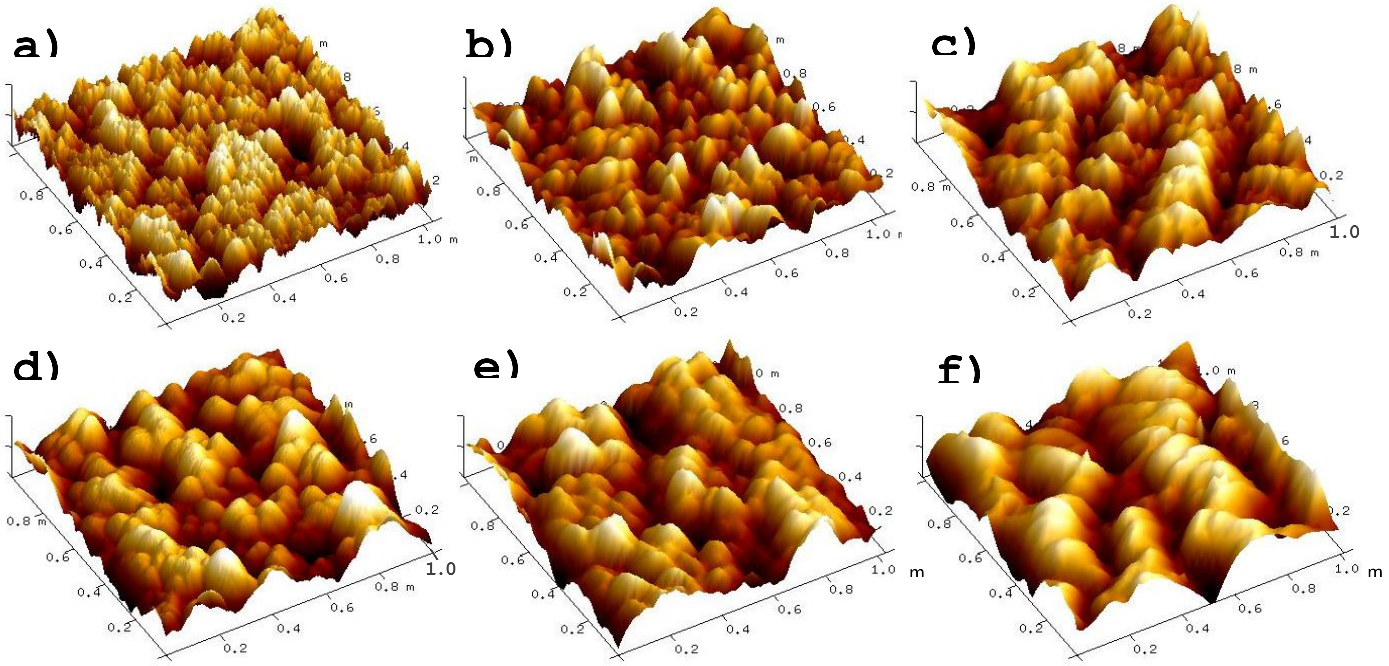

Figure 6: AFM 3D images showing the surface profile of (a) 2 coats sample made from 90 °C sol (b) 6 coats sample made from 90 °C sol (c) 2 coats sample made from 90 °C sol (d) 2 coats sample made from 180 °C sol (e) 6 coats sample made from 180 °C sol (f) 12 coats sample made from 180 °C sol

The roughness of the prepared samples varies with increasing number of coating cycles. This nature was observed for the samples prepared for both the sol. For samples prepared from 90 °C sol, RMS roughness was observed to be ~3 nm, ~9 nm and ~13 nm for 2 coats, 6 coats and 12 coats samples respectively. For the similar kind of samples, Rq increases to ~15 nm, ~19 nm and ~23 nm when the sol preparation temperature is increased to 180 °C. The values of average roughness for the mentioned samples are ~2 nm, ~7 nm, ~10 nm, ~12 nm, ~15 nm and ~18 nm respectively. Sample roughness (both Ra and Rq) increases as sol preparation temperature increases. This increment might be a result of bigger particle size and improved crystalline nature of the films[34,35]. Lin et al36 described that the high temperature can hasten the migration of grain boundaries resulting in the coalescence of grains. PL studies of our samples showed that higher sol preparation temperature leads to oxygen deficient films which leads to higher roughness values for the samples, as suggested by Izadneshan et. al[37.]

Large grain size and high porosity of the deposited films are responsible for this increased roughness at larger thickness values.

If the particle distribution on a surface follows a Gaussian profile, Ra and Rq are related as:

$$R_q \approx \sqrt{\frac{\pi}{2}} R_a \approx 1.25 \times R_a \tag{2}$$

i.e., according to the statistical theory, Rq/Ra should be 1.2538. Since the values of Rq/Ra for the present samples are reasonably close to 1.25 (Table 1), we can assume the surfaces to have Gaussian height distribution, at the imaging scale,.

Besides surface roughness, we also evaluated the surface skewness and kurtosis. The definition of surface skewness (Rsk) is as follow39,

$$R_{sk} = \frac{1}{R_q^3} \frac{1}{N} \sum_{i=0}^{N} Z_i^3 \tag{3}$$

Skewness is a dimensionless quantity, which in general is evaluated as positive or negative values. For negative skewness, the valleys are dominant over the scanned area, and the peaks are dominant when it is positive. Our samples are valley dominant as all of them possess negative skewness values.

Kurtosis (Rku) is mathematically directly related to the peak heights and valley depths according to the following formula:

$$R_{ku} = \frac{1}{R_q^4} \frac{1}{N} \sum_{i=0}^{N} Z_i^4 \tag{4}$$

Where Z is the profile height at the point number i. When Rku value for a surface is <3, it indicates that the scanned area has relatively less numbers of high peaks and low valleys, indicative of a bumpy surface. When Rku is greater than three, the surface will have higher numbers of high peaks and deep valleys, characterizing a spiky surface. All our samples appear to follow the first case which is also evident from the AFM 3D images[40].

Ra, Rq, Rsk, Rku, crystallite size (D, measured from XRD) and average agglomeration size (measured from FESEM images) of the samples are summarized in the following table and the corresponding graphical representation is shown in figure7.

Table 2: Tabular representation of RMS roughness, average roughness, skewness and kurtosis of all the samples

Sample Name	R_q (nm)	R_a (nm)	R_q/ R_a	R_{sk}	R_{ku}
90 deg_2 coats	2.68	2.18	1.23	-0.3444	-0.18753
90 deg_6 coats	9.26	7.38	1.25	-0.14083	0.14693
90 deg_12 coats	13.418	10.50	1.27	-0.12454	0.32967
180 deg_2 coats	14.99	11.89	1.26	-0.19587	0.35046
180 deg_6 coats	19.28	15.49	1.24	-0.26284	0.2438
180 deg_12 coats	23.33	18.55	1.26	-0.30022	0.23645

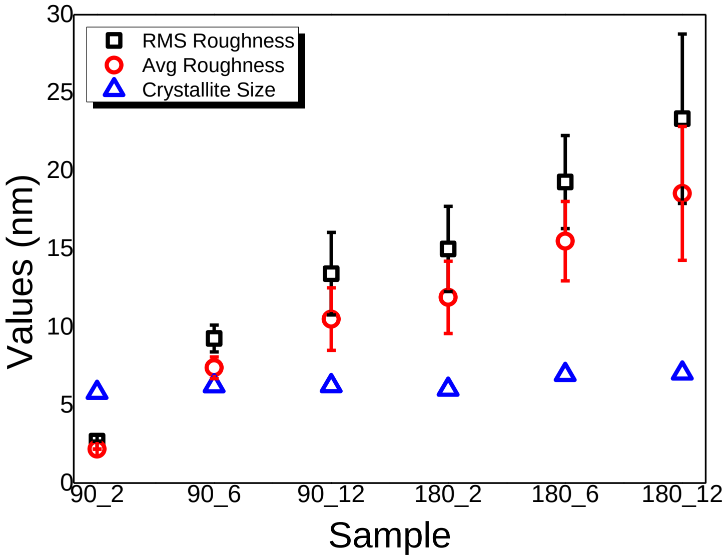

Figure 7: Graphical representation of (a) RMS roughness and (b) Average roughness and (c) crystallite size of the TiO_2 thin films obtained from AFM data and XRD profile with their corresponding AFM 2D images

The depth histogram of the nanoparticles has been depicted in figure 8. The width of the histograms increases continuously with increase in film thickness and their peaks shift towards higher values. This nature is consistent with particle size distribution obtained from the FESEM study.

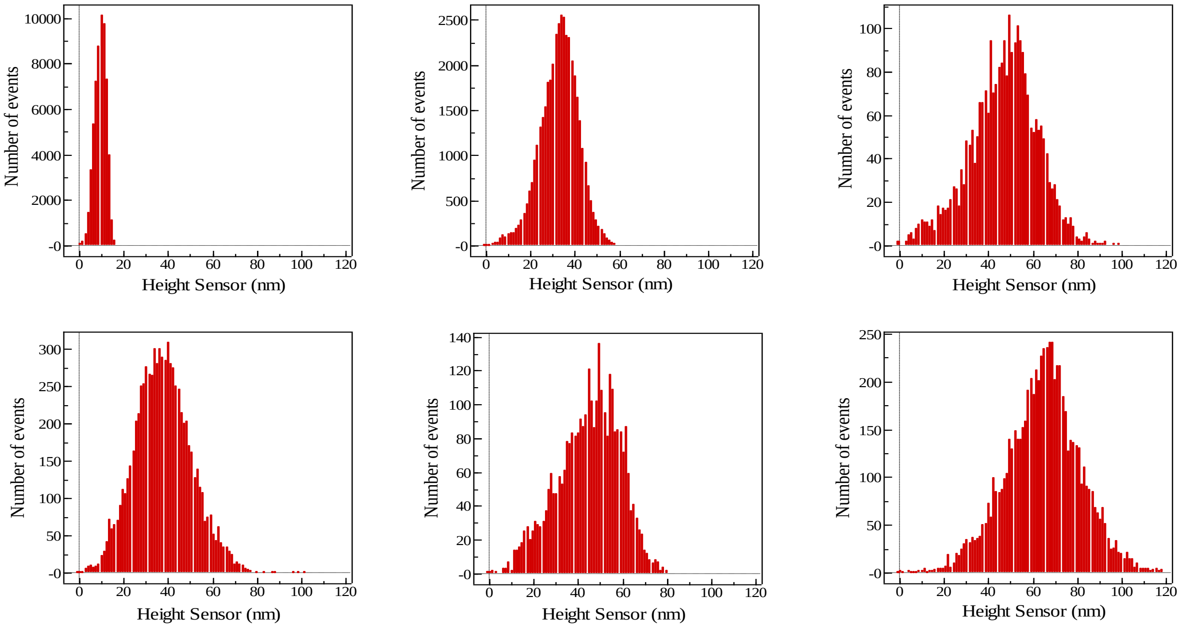

Figure 8: AFM height histogram of samples made from 90 °C sol (a) 2 coats (b) 6 coats (c) 12 coats and samples made from 180 °C sol (d) 2 coats (e) 6 coats (f) 12 coat

3.5 Optical properties:

Thin films show a gradual rise in transmittance (Figure 9) starting at the violet-ultraviolet transition region from almost zero to maximum of ~55% in the visible region. This maximum transmittance value was observed for samples with 2 coats made from both the sols and it decreases with increased number of coating cycles. FESEM images reveal that, particle size increase with increased number of coatings and this eventually increase the surface roughness and amount of scattered light. Also increased thickness enhances the amount of absorbed light. At higher sol preparation temperature, presence of a large number of oxygen vacancies absorbs the incident light which also leads to decrease in transmittance.

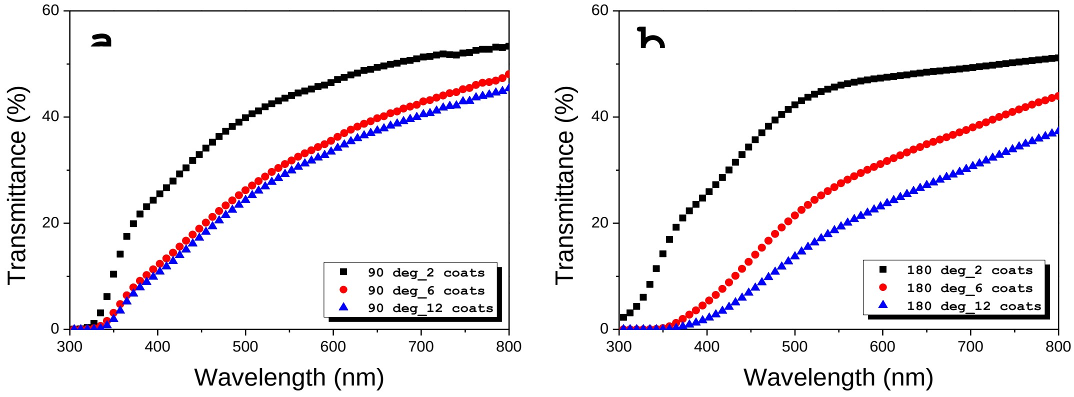

Figure 9: Optical Transmittance spectra of (a) samples made from 90 °C sol and (b) samples made from 180 °C sol

The optical band gap (*Eg*) of the TiO_2 films was calculated using the following relation;

$$(\alpha h\nu)1/2 = \text{const.} \times (h\nu - Eg) \qquad (5)$$

Where α is the absorption coefficient. Figure 10 depicts the relationship between $(\alpha h\nu)1/2$ vs photon energy $h\nu$ of the TiO_2 films. The optical band gap of the films was determined by extrapolating the linear portion of the curves to the energy axis. For the films made from 90 °C sol the values were found to be 3.24 eV, 3.15 eV and 3.16 eV for 2 coats, 6 coats and 12 coats samples respectively. For the same kind of films made from 180 °C sol, the values are 2.85 eV, 2.87 eV and 2.98 eV respectively. The band gap decreased for when sol preparation temperature was increased, but for the film made from the same sol there is no considerable change in the band gap value. Larger particle size and thermal stress in the films at higher sol preparation temperature leads to band gap decrement. The increase in particle size is clearly observed in the FESEM images.

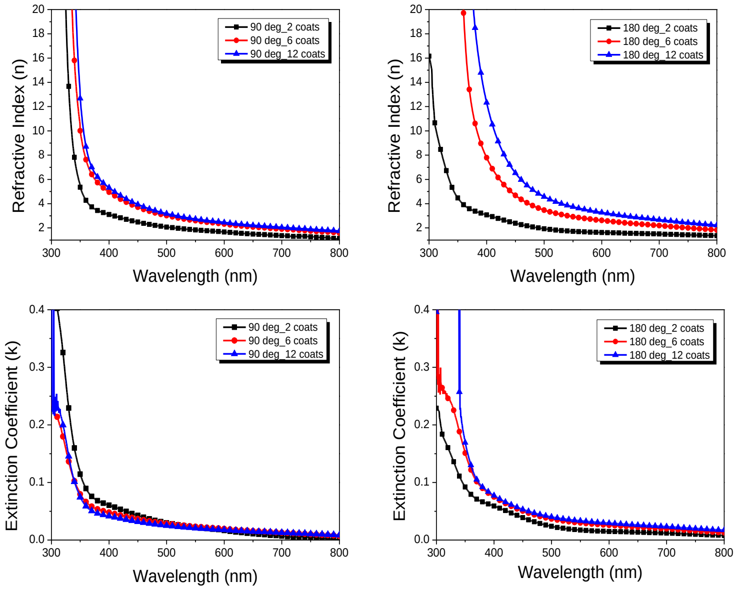

Figure 10: Refractive Index Extinction Coefficient of samples made from (left) 90 °C sol and (right) from 180 °C sol

The tailing of disordered states near the band edges are generally characterized by the Urbach energy, given by the exponential equation:

$$\alpha = \alpha_0 exp\frac{h\nu}{E_u} \qquad (6)$$

Or,

$$ln\alpha = ln\alpha_0 + \frac{h\nu}{E_u} \qquad (7)$$

We calculated the Urbach Energy from the slope of the linear portion of lnα vs. hν of the samples. For samples made from 90 °C sol Urbach energy values were 293 meV, 345 meV and 300 meV for 2 coats, 6 coats and 12 coats samples. For the other batch of samples the values were 380 meV, 340 meV and 440 meV. It can be observed that Urbach energy values are slightly larger in case of samples made from higher temperature sol. It means more energy level due to the disorderness smears into the band edges causing the observed narrowing of band gap values. For all the samples low Urbach Energies suggest good crystalline nature as already observed in the XRD studies.

Refractive indices and the extinction co-efficient of the deposited films were calculated from the reflectance data using the following formulae41,

$$n = \frac{1+\sqrt{R}}{1-\sqrt{R}} \qquad (8)$$

And[42]

$$k = \frac{\alpha\lambda}{4\pi} \qquad (9)$$

Both the refractive indices and extinction co-efficients show exponentially decreasing nature throughout the observed wavelength range. The spectral dependence these parameters are shown in figure 10. In the lower wavelength region (i.e. higher incident energy) due to resonance phenomenon between the incident electromagnetic radiation and the electron polarization in the material coupling of electrons take place. This leads to attenuation in propagation of electromagnetic wave through the material. Thus, both refractive index and extinction coefficient showed higher values at lower wavelength region. Mott and Davis have mentioned a similar trend for many others of amorphous semiconductor thin films[43,44]. The refractive index and the extinction coefficient decreases with the increasing wavelength as less amount of photon are absorbed at lower energy. Refractive index values increase with increase in film thickness. This is because of increase in film density as a result of the imposition of new layers. The values of refractive indices at wavelength 633 nm are 1.55, 2.15, 2.29, 1.57, 2.45 and 3 for 2, 6, 12 coat samples made from 90 °C sol and 180 °C sol respectively (Figure 11). Extinction coefficient also show similar behavior. Samples from 90 °C sol do not show much variation of extinction coefficient over the observed spectral range. But samples from other sol show a little increment with increased film thickness. Increased number of deposition layers also increases film roughness as observed in AFM studies which in term causes enhance scattering from the surface imperfections. This scattering loss leads to increased extinction coefficient.

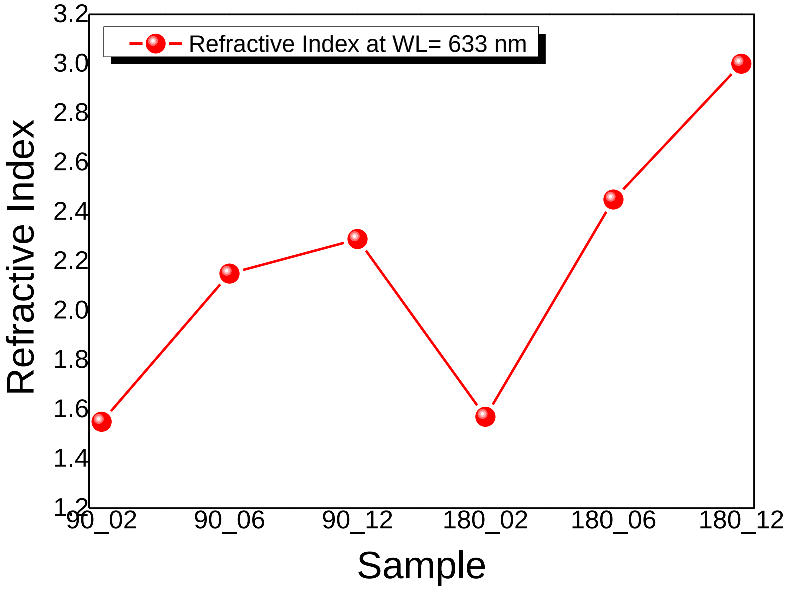

Figure 11: Refractive Index value at wavelength 633 nm of samples made from 90 °C sol and 180 °C sol

The obtained values of *n* and *k* were used to calculate both real ε_r and imaginary parts ε_i of the dielectric constant and they were obtained using the formulas45:

$$\varepsilon_r = n^2 - k^2 \qquad (10)$$

$$\varepsilon_i = 2nk \qquad (11)$$

The real part, ε_r, gives an idea about maximum amount of energy that can be stored in the material and ε_i is about the energy loss. The variation of both real ε_r and imaginary ε_i parts of the dielectric constant with the incident wavelength for all TiO_2 samples are shown in Figure 12.

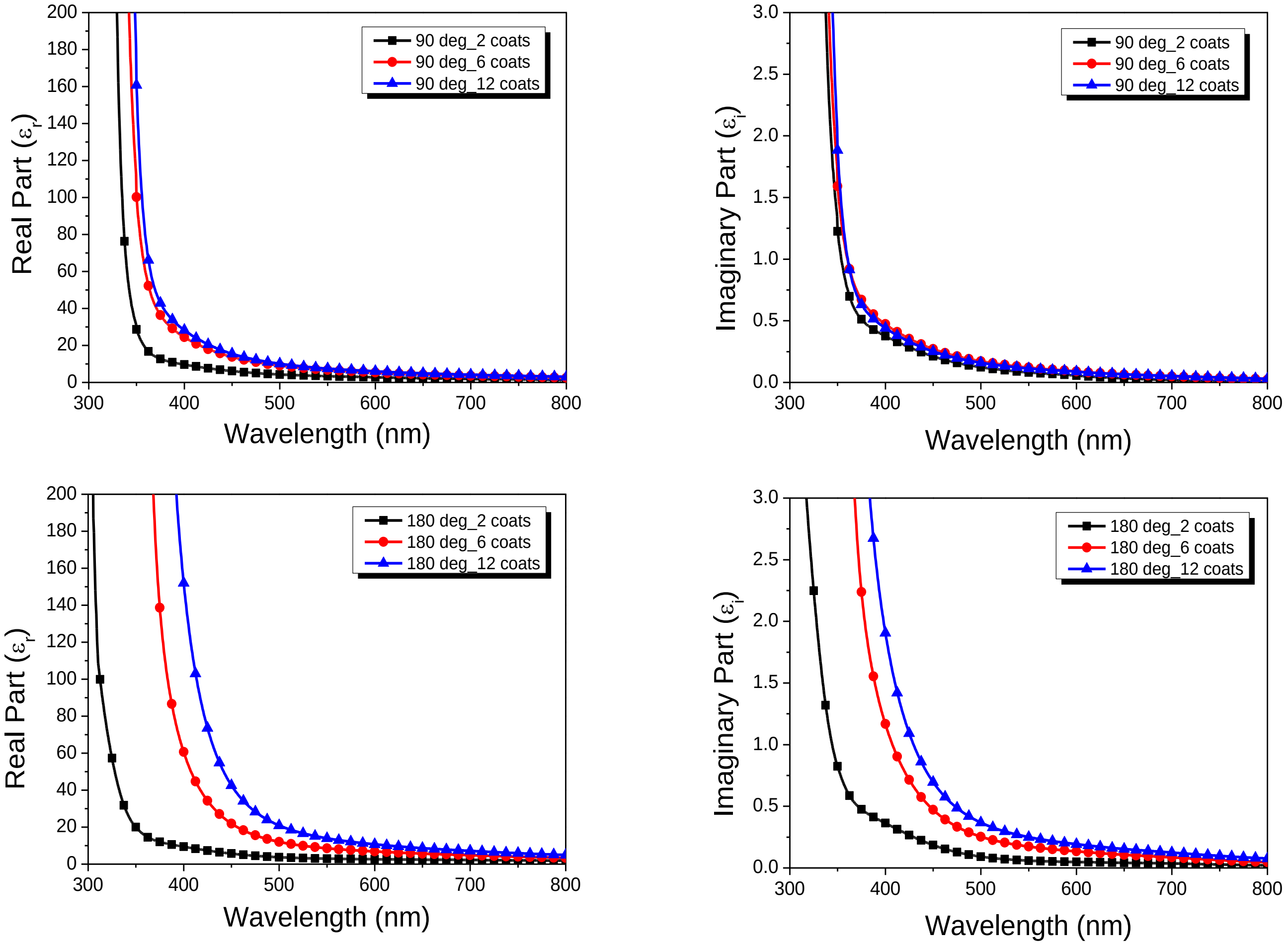

Figure 12: Real and Imaginary part of the dielectric constants of samples made from (left) 90 °C and (right) 180 °C sol

It can be noticed that the values of the real part are higher than those of the imaginary part, they show similar spectral nature. Both the real and imaginary part of the dielectric constant, decrease in an exponential manner with wavelength. Real part of the dielectric constant mostly depends on n2, thus similar to refractive index, samples with highest thickness show highest values of dielectric constant, both real and imaginary part. On application of external electric field space–charge polarization occurs and a large number of dipole moments are formed and trapped by defect states present in the films. Presence of large number of defect states, especially oxygen vacancy related defects triggers up this dipole formation. Thus thicker films possess higher values of dielectric constants due to higher number of oxygen vacancies. Dutta et al.46 calculated the dielectric properties of the related material ZrO_2 with and without oxygen vacancies and observed doubling of dielectric constant when oxygen vacancies were present. At higher frequencies (at lower wavelength) besides space charge polarization, other polarizations also come into effect increasing the value of dielectric constants at higher frequencies.

Tangent loss or dielectric loss (tan δ) gives us an idea about the nature of electromagnetic in a material.

$$tan\delta = \frac{\varepsilon_i}{\varepsilon_r} \qquad (12)$$

The angle δ is the phase difference between the incident radiation and the radiation propagating through the material. Higher value of this parameter indicates that the charge carriers are more free to move inside the material which happened for the thinnest samples in our case (figure 13). For thicker ones, crystallite size increases and the grain boundaries expands as well. This provides a possibility of accumulation of more space charge at these boundaries. As thickness increases, higher amount of oxygen defects trap the charge carrier and thus show lower value of tangent loss.

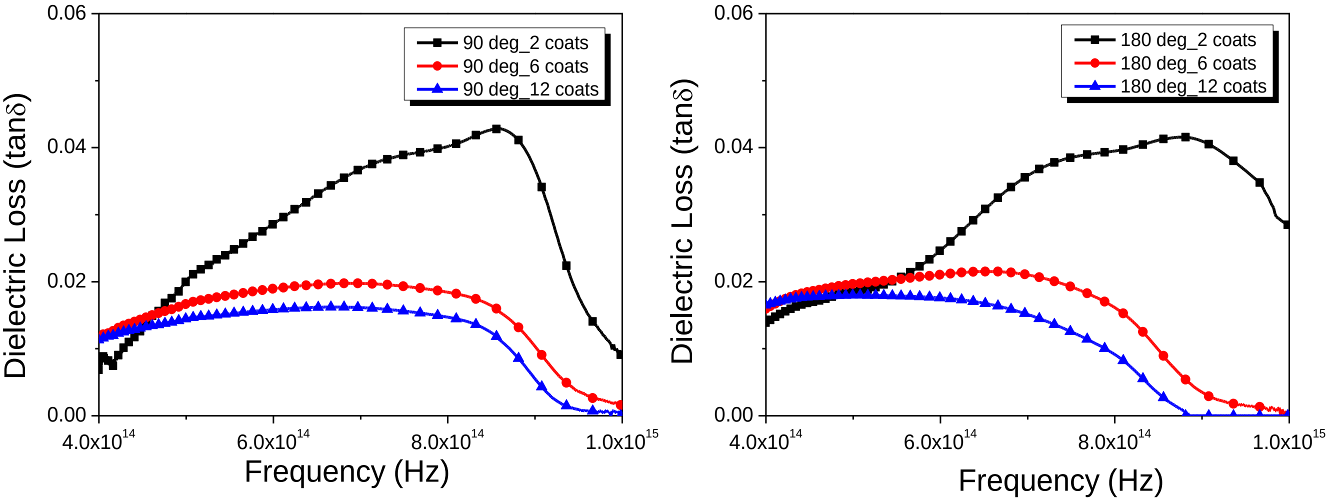

Figure 13: Dielectric Loss of samples made from (a) 90 °C sol and (b) 180 °C sol

3.6 Photoluminescence Spectroscopy:

Photoluminescence Spectroscopy was carried out to further investigate the optical transitions occurring in the films. Figure 14 shows the PL emission spectra of the films made from both the sols in the wavelength range 310 nm — 600 nm. In this range several well-resolved PL peaks were observed. The band to band transitions were observed at 370 nm and 380 nm for samples made from 90 °C sol and 180 °C sol respectively. The most intense peak was observed at 442 nm for both kinds of samples. The other peaks were also observed at the same wavelength for samples made from both the sols at 397 nm, 422 nm, 465 nm, 483 nm and 536 nm. Presence of these large number of PL peaks are indicative for abundance of surface defect states in all the samples.

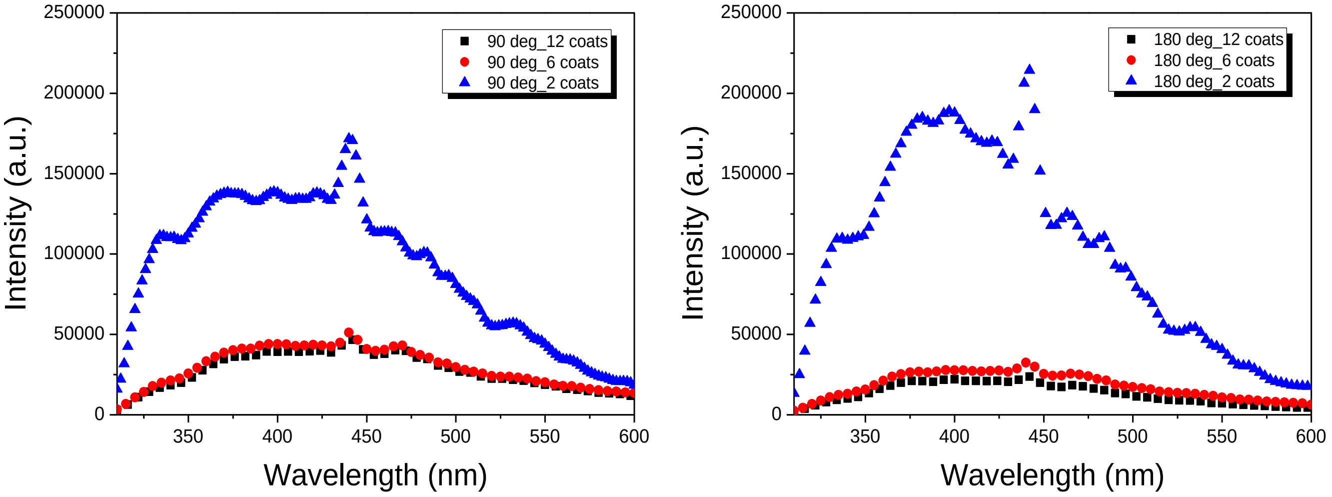

Figure 14: Photoluminescence emission spectra of samples made from (a) 90 °C sol and (b) 180 °C sol

As stated, 370 nm and 380 nm peaks corresponds to band edge transitions. The red shift of band edge peaks for samples made from higher temperature sol due to bigger particle sizes confirmed by the XRD study as well. Band gap study from UV-Vis spectroscopy has also confirmed this red shift. Other peaks are related to different kind of defect levels mostly related to the surface states and present within the forbidden gap[47]. Theoretical studies suggested that a high concentration of electron vacancy and self trapped excitons (STE) can induce an electronic level just below the conduction band[48]. STEs are the conditions when photogenerated excitons are trapped in lattice defects and unable to move through the lattice According to past studies, 397 nm and 422 nm peaks are the result of the charge-transfer transition from Ti3+ to oxygen anion in a TiO_6^{8-} complex[49],. Zuo et al.[50] also reported the presence of such kind of band related to the oxygen vacancy associated with Ti^{3+} just below the conduction band minima. The highest intensity peak was observed at 442 nm. This is mostly related to the shallow trap states present near the band edge.[51]. The emission bands at 452 nm and 473 nm for all the samples indicates the transition involving surface states and occurs due to the recombination of trapped electron–hole arising from unsaturated bonds in the TiO_2 nanoparticles on the surface. When some titanium atoms are exposed to the surface region of thin film and changed into Ti^{3+}, Ti^{2+}, Ti^{+}, localized energy levels are introduced within the forbidden gap. Several small peaks were observed in the wavelength range 460-560 nm. These peaks mainly result from the oxygen vacancies. Shi et. al.[52] observed this visible band to quench after annealing in oxygen rich atmosphere and enhance after reduction in H_2. And thus concluded this band is due to oxygen vacancy.

PL intensity was found to decrease with increasing thickness. From XRD data we observed that, crystallite size (and the grain size as well) increases with increase in film thickness. In general, the density of the surface states decreases with the grain size increase and luminescence intensity decreases with decrease of the density of the surface states. Also thicker films, due to their rough nature and presence of more voids, results in more dangling bonds at the surface creating electronic states in the forbidden gap region which act as centres for non-radiative recombination, quenching the PL intensities. PL intensity increases with increasing sol preparation temperature for the thinnest film only and for the rest of the films the intensities are almost comparable. FESEM images of our samples reveal that TiO_2 particle size increases with increasing sol preparation temperature along with the introduction of some voids in the films. Therefore, surface area exposed to the environment is also enhanced. Increment in the surface roughness, as measured from AFM, also support this fact. At the surface region of the film, titanium atoms are changed into Ti^{3+}, Ti^{2+}, Ti^{+} and some localized energy levels are formed within the forbidden gap. With more exposed surface radiative recombination at these localized levels becomes more intense leading to increment in PL intensity. For the thinnest film electrons generated inside the materials quickly move to the promoting the recombination further. But as the sol preparation temperature rises, another phenomenon that affects the occurrence of these defect levels is the improvement in crystallization. XRD peaks support this fact and due to this intrinsic defects are healed causing reduced number of radiative recombination pathways. For 6 and 12 times coated samples this improvement is even more overcoming the increased surface defects and prohibiting the PL intensity enhancement.

On the basis of the PL emission spectra of the samples shown in figure 15, we calculated the chromaticity co-ordinates (CIE 1931) of all the samples . All the samples were observed to fall in the blue region. This indicates the high UV activity of all three samples and the samples should be efficient for UV light driven photocatalytic activity.

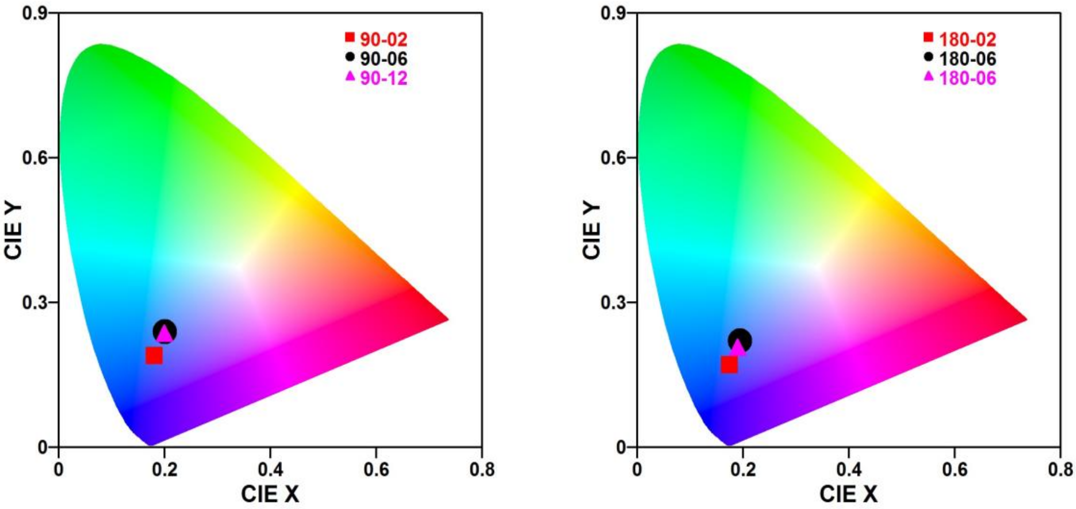

Figure 15: Chromaticity diagram of (a) samples made from 90 °C sol and (b) samples made from 180 °C sol

3.7 Photocatalytic Activity:

The photodegradation of Methylene Blue dye by TiO_2 photcatalysts is a pseudo-first-order reaction where the photodegradation rate constant (k) can be determined by the following equation:

$$ln\frac{C_t}{C_0} = -kt \qquad (13)$$

Where C_0 and C_t are the initial concentration and the concentration at time t of the dye solution, respectively, and k is the first-order rate constant. A plot of ln C_0/C_t vs time represented in figure 16 yields a linear nature, slope of which upon linear regression determines the first-order rate constant k. Higher values of k indicates better degradation.

The degradation rate of the dye is generally expressed as,

$$Degradation\ Rate = \frac{C_0 - C_t}{C_0} \qquad (14)$$

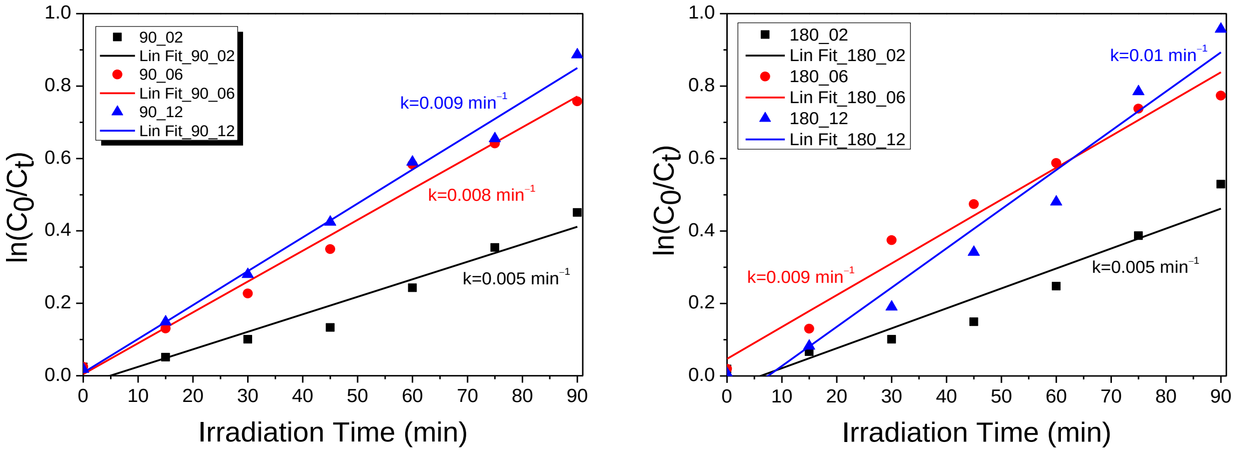

Figure 16: Determination of rate constant for photodegradation of dye with catalyst made from (a) 90 °C sol and (b) 180 °C sol

The photocatalytic activity of the prepared samples increase as the number of coating increases. But for same coatings, it does not show much variation with the change in hydrothermal temperature. For samples made from 90 °C sol, degradation of dye after 90 min are 36%, 53% and 59% for coating cycles 2, 6 and 12 respectively. These values changes to 41%, 54% and 62% when the sol preparation temperature was increased to 180 °C. It means that degradation rate increases with increasing film thickness irrespective of the sol preparation temperature. Increasing sol temperature also enhances the rate, but only a little and mostly for the thinnest film. Degradation of the dye after 90 min and the kinetic rate for each sample has been represented in figure 17.

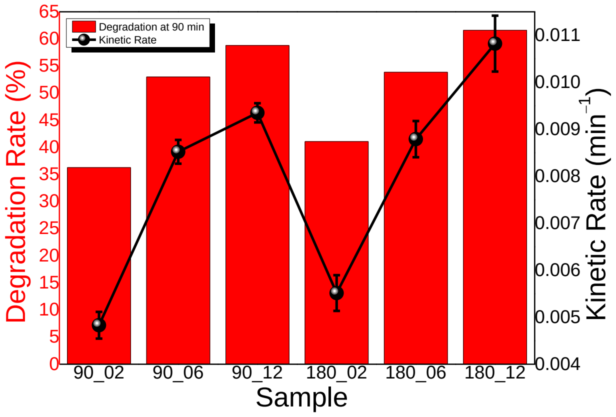

Figure 17: Degradation rate and the kinetic rate of photo degradation of samples made from 90 °C sol and 180 °C sol

Dye degradation mainly depends on the successful separation of photo induced electron-hole pair in the photocatalyst which results in the oxidization of the aqueous solvent and creates the hydroxyl ion which gets attached to the active sites on the surface of the thin films under suitable light irradiation. The produced OH● radicals then attack the R–S+=R functional group in the Methylene Blue dye and results in the cleavage of bonds of the group into R–S(=O)–R, $R–SO_2–R$, $R–SO_3H–R$ etc. finally to degrade the dye[53]. Penetration depth of UV light is very low (δp≈100 nm). So photocatalysis is essentially a surface phenomenon and thus closely related to PL. The PL peak intensity of the investigated thin films reduces with increase in film thickness for films made from both the sols indicating less amount of radiative recombination of e−/h+ pair as explained earlier. In thinner films the e−/h+ pair generated deep inside the bulk quickly reach the surface and surface recombination becomes a predominant process, as this is much faster than bulk recombination. Availability of enough surface defect sites plays a crucial role here. It justifies the enhancement of photocatalytic activity of the films with their increasing thickness. FESEM images confirm that on increasing sol temperature particle size increases with introduction of void in the films and increase in film roughness providing more effective surface area and consecutively more number of active sites available to enhance the degradation pathway and thus increasing the degradation rate. With increase in sol preparation temperature, band gap values for the samples decreases. Lower band gap value leads to the possibility of more light absorption which in terms enhance electron-hole pair generation and also the photocatalytic activity. Better crystallinity at higher sol preparation temperature also contributes to this.

The Materials and Methods should be described with sufficient details to allow others to replicate and build on the published results. Please note that the publication of your manuscript implicates that you must make all materials, data, computer code, and proto-cols associated with the publication available to readers. Please disclose at the submission stage any restrictions on the availability of materials or information. New methods and protocols should be described in detail while well-established methods can be briefly de-scribed and appropriately cited.

Research manuscripts reporting large datasets that are deposited in a publicly avail-able database should specify where the data have been deposited and provide the relevant accession numbers. If the accession numbers have not yet been obtained at the time of submission, please state that they will be provided during review. They must be provided prior to publication.

Interventionary studies involving animals or humans, and other studies that require ethical approval, must list the authority that provided approval and the corresponding ethical approval code.

4. Conclusions

Titania thin films were prepared by sol-gel dip coating method. The sol was synthesized by hydrothermal method in a Teflon lined stainless steel autoclave separately at two different temperatures, viz. 90 ºC and 180 ºC for 12 h each. All the samples were deposited by repeating the dipping cycle 2, 6 and 12 times to vary their thickness and later all of them were annealed at 500 ºC for 6h. The XRD profiles revealed that, anatase phase was formed in all the samples which is the most suitable form of TiO_2 for photocatalytic activity, according to past researches. Crystallite size as calculated from the XRD peaks, showed a little increment with film thickness and as well as at higher sol preparation temperature. All the films are composed of spherical morphology and the agglomeration size increases with film thickness and the sol preparation temperature as well. For films with similar coatings particle size increment is clearly visible for samples made from higher temperature sol. These agglomeration of nanoparticles have narrower size distribution for lower thickness. Surface morphology was also observed by Atomic force microscopy which shows that, both RMS (Rq) and average surface roughness (R_a) increases with increased sol preparation temperature and thickness in the similar manner. R_q and R_a maintains a constant ratio of ~1.25 for each and every sample. UV-Vis spectroscopy reveals, the films exhibit almost zero transmittance at violet-ultraviolet transition region and then have a gradual rise up to ~55% at the near Infrared. All the samples exhibit similar nature of transmittance. Transmittance value decreases slightly as sol preparation temperature is increased. But considerable decrement in transmittance value is observed for thicker samples. Band gap values for all the samples do not show any significant difference when film thickness is varied. But with increased sol preparation temperature, it shows a decrement. Photoluminescence spectra show the appearance of several peaks in the wavelength range 310 − 600 nm. Most of the peaks are due to defect states related to oxygen vacancy and self-trapped excitons. All the samples exhibit similar PL nature. Intensity of PL peaks gets enhanced with decreasing thickness indicating less number of defect sites and reduced radiative recombination in those samples. Effect of this phenomenon was also observed in the photo degradation of Methylene Blue dye. The degradation rate was found to increase with increasing film thickness for samples made from both the sols.

Data accessibility:

The data will be available on request

Conflict of interest declaration:

There is no conflicts of interest

Acknowledgements:

Authors are grateful to Central Research Facility (CRF), IIT (ISM) Dhanbad for providing UV-Vis NIR spectroscopy, FESEM and AFM facility. We also acknowledge DST-FIST facility (project no. SR/FST/PSI-004/2013) of Depertment of Physics, IIT (ISM) Dhanbad for providing us the photoluminescence spectrometer. FTIR was carried out at Meghnad Saha Institute of Technology, Kolkata under the guidance of Prof. Utpal Ganguly and we are grateful to him for his support.

1 References

1. Jung, H. S., & Lee, J. K. (2013). Dye sensitized solar cells for economically viable photovoltaic systems. *The journal of physical chemistry letters*, *4*(10), 1682-1693.
2. O'regan, B., & Grätzel, M. (1991). A low-cost, high-efficiency solar cell based on dye-sensitized colloidal TiO2 films. *nature*, *353*(6346), 737-740.
3. Tachikawa, T., Fujitsuka, M., & Majima, T. (2007). Mechanistic insight into the TiO2 photocatalytic reactions: design of new photocatalysts. *The Journal of Physical Chemistry C*, *111*(14), 5259-5275.
4. Kadoshima, M., Hiratani, M., Shimamoto, Y., Torii, K., Miki, H., Kimura, S., & Nabatame, T. (2003). Rutile-type TiO2 thin film for high-k gate insulator. *Thin Solid Films*, *424*(2), 224-228.
5. Wang, J., Polleux, J., Lim, J., & Dunn, B. (2007). Pseudocapacitive contributions to electrochemical energy storage in TiO2 (anatase) nanoparticles. *The Journal of Physical Chemistry C*, *111*(40), 14925-14931.
6. Ochiai, T., & Fujishima, A. (2012). Photoelectrochemical properties of TiO2 photocatalyst and its applications for environmental purification. Journal of Photochemistry and photobiology C: Photochemistry reviews, 13(4), 247-262.
7. Khan, S. U., Al-Shahry, M., & Ingler, W. B. (2002). Efficient photochemical water splitting by a chemically modified n-TiO2 Science, 297(5590), 2243-2245.
8. Lu, H. F., Li, F., Liu, G., Chen, Z. G., Wang, D. W., Fang, H. T., ... & Cheng, H. M. (2008). Amorphous TiO2 nanotube arrays for low-temperature oxygen sensors. *Nanotechnology*, *19*(40), 405504.
9. Kwon, D. H., Kim, K. M., Jang, J. H., Jeon, J. M., Lee, M. H., Kim, G. H., ... & Kim, M. (2010). Atomic structure of conducting nanofilaments in TiO2 resistive switching memory. Nature nanotechnology, 5(2), 148-153.
10. Braun, J. H., Baidins, A., & Marganski, R. E. (1992). TiO2 pigment technology: a review. Progress in organic coatings, 20(2), 105-138
11. Huang, J., Shinohara, T., & Tsujikawa, S. (1999). Protection of carbon steel from atmospheric corrosion by TiO2 coating. Zairyo-to-Kankyo, 48(9), 575-582
12. Richards, B. S. (2003). Single-material TiO2 double-layer antireflection coatings. Solar Energy Materials and Solar Cells, 79(3), 369-390.
13. Negishi, N., Iyoda, T., Hashimoto, K., & Fujishima, A. (1995). Preparation of transparent TiO2 thin film photocatalyst and its photocatalytic activity. Chemistry Letters, 24(9), 841-842.
14. Yu, J., Zhao, X., & Zhao, Q. (2000). Effect of surface structure on photocatalytic activity of TiO2 thin films prepared by sol-gel method. *Thin solid films*, *379*(1-2), 7-14.
15. Yu, J., Zhao, X., & Zhao, Q. (2001). Photocatalytic activity of nanometer TiO2 thin films prepared by the sol–gel method. *Materials Chemistry and Physics*, *69*(1-3), 25-29.
16. Wang, Z., Helmersson, U., & Käll, P. O. (2002). Optical properties of anatase TiO2 thin films prepared by aqueous sol–gel process at low temperature. *Thin Solid Films*, *405*(1-2), 50-54.
17. Kasuga, T., Hiramatsu, M., Hoson, A., Sekino, T., & Niihara, K. (1998). Formation of titanium oxide nanotube. Langmuir, 14(12), 3160-3163.
18. Ichinose, H., Terasaki, M., & Katsuki, H. (2001). Properties of peroxotitanium acid solution and peroxo-modified anatase sol derived from peroxotitanium hydrate. Journal of Sol-Gel Science and Technology, 22(1), 33-40.
19. Lee, C. K., Kim, D. K., Lee, J. H., Sung, J. H., Kim, I., Lee, K. H., ... & Lee, Y. K. (2004). Preparation and characterization of peroxo titanic acid solution using TiCl3. Journal of sol-gel science and technology, 31(1), 67-72.
20. Li, W., Bai, Y., Liu, C., Yang, Z., Feng, X., Lu, X., … Chan, K.-Y. (2009). Highly Thermal Stable and Highly Crystalline Anatase TiO2for Photocatalysis. Environmental Science & Technology, 43(14), 5423–5428.
21. Biswas, S., Jiménez, C., Khan, A., Forissier, S., Kar, A. K., Muñoz-Rojas, D., & Deschanvres, J. L. (2017). Structural study of TiO 2 hierarchical microflowers grown by aerosol-assisted MOCVD. *CrystEngComm*, *19*(11), 1535-1544.
22. Pedemonte, M. M., Visintin, A., & Capparelli, A. L. (2010). Study of a photostable thin films of TiO2 on titanium. *International journal of hydrogen energy*, *35*(11), 6069-6073.
23. Zhou, X., Yu, S., Jiao, S., Lv, Z., Liu, E., Zhao, Y., & Cao, N. (2019). Fabrication of superhydrophobic TiO2 quadrangular nanorod film with self-cleaning, anti-icing properties. *Ceramics International*, *45*(9), 11508-11516.

---

24. Lettieri, M., Colangiuli, D., Masieri, M., & Calia, A. (2019). Field performances of nanosized TiO2 coated limestone for a self-cleaning building surface in an urban environment. *Building and Environment*, *147*, 506-516.
25. Wang, Y., Zhang, L., Deng, K., Chen, X., & Zou, Z. (2007). Low temperature synthesis and photocatalytic activity of rutile TiO2 nanorod superstructures. *The Journal of Physical Chemistry C*, *111*(6), 2709-2714.
26. Yurdakal, S., Palmisano, G., Loddo, V., Augugliaro, V., & Palmisano, L. (2008). Nanostructured rutile TiO2 for selective photocatalytic oxidation of aromatic alcohols to aldehydes in water. *Journal of the American Chemical Society*, *130*(5), 1568-1569.
27. Ge, L., Xu, M., Fang, H., & Sun, M. (2006). Preparation of TiO2 thin films from autoclaved sol containing needle-like anatase crystals. Applied Surface Science, 253(2), 720-725.

29. Ben Yahia, M., Lemoigno, F., Beuvier, T., Filhol, J. S., Richard-Plouet, M., Brohan, L., & Doublet, M. L. (2009). Updated references for the structural, electronic, and vibrational properties of TiO2 (B) bulk using first-principles density functional theory calculations. *The Journal of chemical physics*, *130*(20), 204501.
30. Ivanda, M., Musić, S., Popović, S., & Gotić, M. (1999). XRD, Raman and FT-IR spectroscopic observations of nanosized TiO2 synthesized by the sol–gel method based on an esterification reaction. *Journal of Molecular structure*, *480*, 645-649.
31. KO HYY, M. M., KAJINAMI, A., & DEKI, S. (2003). Fabrication of high performance thin films from metal fluorocomplex aqueous solution by the liquid phase deposition [J]. *Journal of Fluorine Chemistry*, *120*, 157-163.
32. Ferraris, J. (1997). L64 J Electrochem. Soc., Vol. 144, No. 4, April 1997 The Electrochemical Society, Inc. *J. Electrochem. Soc*, *144*(4).
33. Li, G., Dimitrijevic, N. M., Chen, L., Nichols, J. M., Rajh, T., & Gray, K. A. (2008). The important role of tetrahedral Ti4+ sites in the phase transformation and photocatalytic activity of TiO2 nanocomposites. *Journal of the American Chemical Society*, *130*(16), 5402-5403.
34. Wang, M., Wang, J., Chen, W., Cui, Y., & Wang, L. (2006). Effect of preheating and annealing temperatures on quality characteristics of ZnO thin film prepared by sol–gel method. *Materials Chemistry and Physics*, *97*(2-3), 219-225.
35. Liu, Y. C., Tung, S. K., & Hsieh, J. H. (2006). Influence of annealing on optical properties and surface structure of ZnO thin films. *Journal of crystal growth*, *287*(1), 105-111.
36. Y. Lin, J. Xie, H. Wang, Y. Li, C. Chavez, S. Lee, S.R. Foltyn, S.A. Crooker, A.K. Burrell, T.M. Mc Cleskey, Q.X. Jia, Thin Solid Films **101**, 492 (2005).
37. Pullman, J. M. (2019). New views of the glomerulus: advanced microscopy for advanced diagnosis. *Frontiers in medicine*, *6*, 37.
38. Kumar, B. R., & Rao, T. S. (2012). AFM studies on surface morphology, topography and texture of nanostructured zinc aluminum oxide thin films. *Digest Journal of Nanomaterials and Biostructures*, *7*(4), 1881-1889.
39. Ling Li, Ling Li, Weidong Chen, Jie Zheng, Linwen Wang, Yan Chen (2016) Characterization of Silver Nanoparticles Thin Films with Various Thicknesses by AFM. *Journal of Materials Science and Chemical Engineering*,**04**,34-39.
40. Williamson, G. K., & Smallman, R. E. (1956). III. Dislocation densities in some annealed and cold-worked metals from measurements on the X-ray debye-scherrer spectrum. *Philosophical magazine*, *1*(1), 34-46.
41. Chiad, S. S. (2015). Optical characterization of NiO doped Fe2O3 thin films prepared by spray pyrolysis method. *International Letters of Chemistry, Physics and Astronomy*, *6*, 50.
42. Eckortova, L. (1977). Physics of Thin Films Plenum Press. *New York and London*.

43. Davis, E. A., & Mott, N. (1970). Conduction in non-crystalline systems V. Conductivity, optical absorption and photoconductivity in amorphous semiconductors. *Philosophical magazine*, *22*(179), 0903-0922.
44. Mott, N. F., & Davis, E. A. (2012). *Electronic processes in non-crystalline materials*. OUP Oxford.
45. F.Buet, J.Olivier-Fourcade, Y.Bensimon, P.Belougne; Complex Impedance Study of ChalcogenideGlasses, Solid StateCommunications, **77**, 29-32 **(1991)**.
46. Dutta, G., Hembram, K. P. S. S., Rao, G. M., & Waghmare, U. V. (2006). Effects of O vacancies and C doping on dielectric properties of ZrO2: A first-principles study. *Applied Physics Letters*, *89*(20).
47. Liu, B., Zhao, X., & Wen, L. (2006). The structural and photoluminescence studies related to the surface of the TiO 2 sol prepared by wet chemical method. Materials Science and Engineering: B, 134(1), 27-31.
48 I. Justicia, P. Ordejon, G. Canto, J. L. Mozos, J. Fraxedes, G. A. Battiston, R. Gerbasi and A. Figueras, *Adv. Mater.*, 2002, 14,

1399

49. Santara, B., Giri, P. K., Imakita, K., & Fujii, M. (2013). Evidence of oxygen vacancy induced room temperature ferromagnetism in solvothermally synthesized undoped TiO2 nanoribbons. Nanoscale, 5(12), 5476-5488.

50 F. Zuo, L. Wang, T. Wu, Z. Zhang, D. Borchardt and P. Feng, *J. Am. Chem. Soc.*, 2010, 132, 11856

51. Abazović, N. D., Čomor, M. I., Dramićanin, M. D., Jovanović, D. J., Ahrenkiel, S. P., & Nedeljković, J. M. (2006). Photoluminescence of anatase and rutile TiO2 particles. *The Journal of Physical Chemistry B*, *110*(50), 25366-25370.

52. Shi, J., Chen, J., Feng, Z., Chen, T., Lian, Y., Wang, X., & Li, C. (2007). Photoluminescence characteristics of TiO2 and their relationship to the photoassisted reaction of water/methanol mixture. *The journal of physical chemistry C*, *111*(2), 693-699.